

Article

Cropland Inundation Mapping in Rugged Terrain Using Sentinel-1 and Google Earth Imagery: A Case Study of 2022 Flood Event in Fujian Provinces

Mengjun Ku ^{1,2}, Hao Jiang ² , Kai Jia ^{2,*} , Xuemei Dai ² , Jianhui Xu ², Dan Li ², Chongyang Wang ²  and Boxiong Qin ²

¹ Department of Surveying Engineering, Guangdong University of Technology, Guangzhou 510006, China; 2112109048@mail2.gdut.edu.cn

² Key Lab of Guangdong for Utilization of Remote Sensing and Geographical Information System, Guangdong Open Laboratory of Geospatial Information Technology and Application, Guangzhou Institute of Geography, Guangdong Academy of Sciences, Guangzhou 510070, China; jianghao@gdas.ac.cn (H.J.); 18728273633@163.com (X.D.); xujianhui306@gdas.ac.cn (J.X.); lidan@gdas.ac.cn (D.L.); wangchongyang@gdas.ac.cn (C.W.); qinboxiong@radi.ac.cn (B.Q.)

* Correspondence: jiakai@mail.bnu.edu.cn

Abstract: South China is dominated by mountainous agriculture and croplands that are at risk of flood disasters, posing a great threat to food security. Synthetic aperture radar (SAR) has the advantage of being all-weather, with the ability to penetrate clouds and monitor cropland inundation information. However, SAR data may be interfered with by noise, i.e., radar shadows and permanent water bodies. Existing cropland data derived from open-access landcover data are not accurate enough to mask out these noises mainly due to insufficient spatial resolution. This study proposed a method that extracted cropland inundation with a high spatial resolution cropland mask. First, the Proportional–Integral–Derivative Network (PIDNet) was applied to the sub-meter-level imagery to identify cropland areas. Then, Sentinel-1 dual-polarized water index (SDWI) and change detection (CD) were used to identify flood area from open water bodies. A case study was conducted in Fujian province, China, which endured several heavy rainfalls in summer 2022. The result of the Intersection over Union (IoU) of the extracted cropland data reached 89.38%, and the F1-score of cropland inundation achieved 82.35%. The proposed method provides support for agricultural disaster assessment and disaster emergency monitoring.

Keywords: flood; Sentinel-1; sub-meter; PIDNet; inundated croplands mapping



Citation: Ku, M.; Jiang, H.; Jia, K.; Dai, X.; Xu, J.; Li, D.; Wang, C.; Qin, B. Cropland Inundation Mapping in Rugged Terrain Using Sentinel-1 and Google Earth Imagery: A Case Study of 2022 Flood Event in Fujian Provinces. *Agronomy* **2024**, *14*, 138. <https://doi.org/10.3390/agronomy14010138>

Academic Editor: Alberto San Bautista

Received: 11 December 2023
Revised: 23 December 2023
Accepted: 3 January 2024
Published: 5 January 2024



Copyright: © 2024 by the authors. Licensee MDPI, Basel, Switzerland. This article is an open access article distributed under the terms and conditions of the Creative Commons Attribution (CC BY) license (<https://creativecommons.org/licenses/by/4.0/>).

1. Introduction

The inundation of cropland has a significant social impact, damaging crops, spreading crop pests and diseases, contaminating the soil and water sources, and destroying cropland infrastructure such as dikes and canals [1]. In addition, farmers are seen as potential contributors to reducing flood risk by using croplands to give more room for water flooding, which involves increasing their exposure [2]. These factors contribute to decreased crop quality and reduced yields, posing an enormous threat to agricultural food security [3]. Accurate information on the distribution of inundated cropland is an important guide for the government to develop disaster relief and mitigation plans, which is important to ensure food security and safeguard farmers' property [4].

However, monitoring cropland inundation in areas of rugged terrain is challenging since the scarcity of in situ measurement networks in those areas hinders flood analysis [5]. The use of remote satellite sensing data, such as optical and radar data, overcomes the limitations associated with measurement networks [6,7]. This approach enables the precise identification of open water bodies [8] and the extraction of flood inundation areas for

mapping [9–11]. However, during heavy rainfall leading to flooding, adverse weather conditions make it difficult to obtain effective optical remote sensing data. Synthetic Aperture Radar (SAR) remote sensing is less affected by weather and offers all-time and all-weather monitoring [12], making it widely applied in flood monitoring research.

Accurate identification of cropland inundation areas with SAR faces challenges, mainly because it is difficult to distinguish flood area from permanent water bodies and radar shadows in SAR images [13,14]. Due to insufficient information, it is difficult to exclude non-flooded areas by relying solely on SAR images and single observation. Researchers have attempted to introduce multiple SAR observations and external remote sensing data, including digital elevation models (DEMs), land use/land cover, and waterbody mask to solve the above problems. S. Grimaldi et al. [12,15] used the Australian Dynamic Land Cover dataset to remove permanent water bodies. Stefan Schlaffer et al. [16] use the Corine Land Cover 2006 (CLC 2006) dataset to extract permanent water bodies and the flood range. Beste Tavus et al. [17] used Sentinel-1 data to create land cover maps and used them as reference images for change monitoring. It can be considered that accurate cropland data can eliminate permanent water bodies and radar shadows. However, existing publicly available cropland data are usually derived from land cover data, such as the United States Department of Agriculture (USDA) Cropland Data Layer (CDL) [18], world/land cover from the European Space Agency (ESA) [19] and the Environmental Systems Research Institute (ESRI) [20] as well as other land cover data [21]. However, most of the existing land cover products are based on Sentinel and Landsat data, and their spatial resolution is not enough for the cropland mapping of rugged terrain [22] since the average area of crop parcels is only 0.1–0.3 hectares in southern China (as prescribed by the standard of well-facilitated capital farmland construction [23]). Therefore, producing high-precision cropland data through higher spatial resolution images combined with deep learning image interpretation technology is of great significance to improving the accuracy of cropland flooding mapping.

Generally, flooded areas have lower backscattering coefficients that present as dark objects in SAR images [21]. Researchers have developed several waterbody identification techniques applied for flood mapping, such as image segmentation [23,24], classification [25,26], flood index [4,27], and change detection [17]. Classification methods can achieve higher accuracy but are limited by the availability of reliable SAR image samples [28]. In disaster emergency response, classification methods lack automation. Jia et al. [29] inspired by the NDVI and NDWI, introduced the Sentinel-1 dual-polarized water index (SDWI) based on SAR image water features [30]. It can effectively suppress shadows and improve the accuracy of water extraction [31]. Furthermore, radar shadows tend to have relatively consistent forms and locations when monitoring with the same type of sensor in the same area. For large-scale flood extent extraction and mapping, change detection (CD) methods provide a high level of automation and can detect changes in multi-temporal remote sensing images [32].

The objective of this study was to develop a method to improve inundated cropland delineation using high spatial resolution cropland masks. The proposed method extracted sub-meter cropland masks by introducing the Proportional–Integral–Derivative Network (PIDNet), and the SDWI method was combined with change detection (CD) to extract cropland inundation areas. The rest of the paper is organized as follows. The materials and methods are provided in Section 2. The experimental results are reported in Section 3. The discussion of key issues is provided in Section 4. Finally, conclusions are shown in Section 5.

2. Materials and Methods

2.1. Study Area Description

The study area is Fujian Province, which is located in southeastern China (Figure 1). It extends from 20°13' N to 25°31' N latitude and 109°39' E to 117°19' E longitude and covers approximately 124,000 km². In total, 89.3% of the province's area is occupied by mountain

and hill areas. Fujian Province has 9319.93 km² of cultivated land, which represents 10.64% of its total area. The cropland features fragmented plots and a diverse range of crops. Typhoons and heavy rain are common in summer and autumn in this region, which has abundant precipitation. The annual average precipitation ranges from 800 to 1900 mm, and the most precipitation occurs during May and June every year. During the study period in June 2022, Fujian Province was hit by heavy rainfall and flooding. Until 20 June, the agricultural losses in the province amounted to approximately CNY 1.69 billion [33].

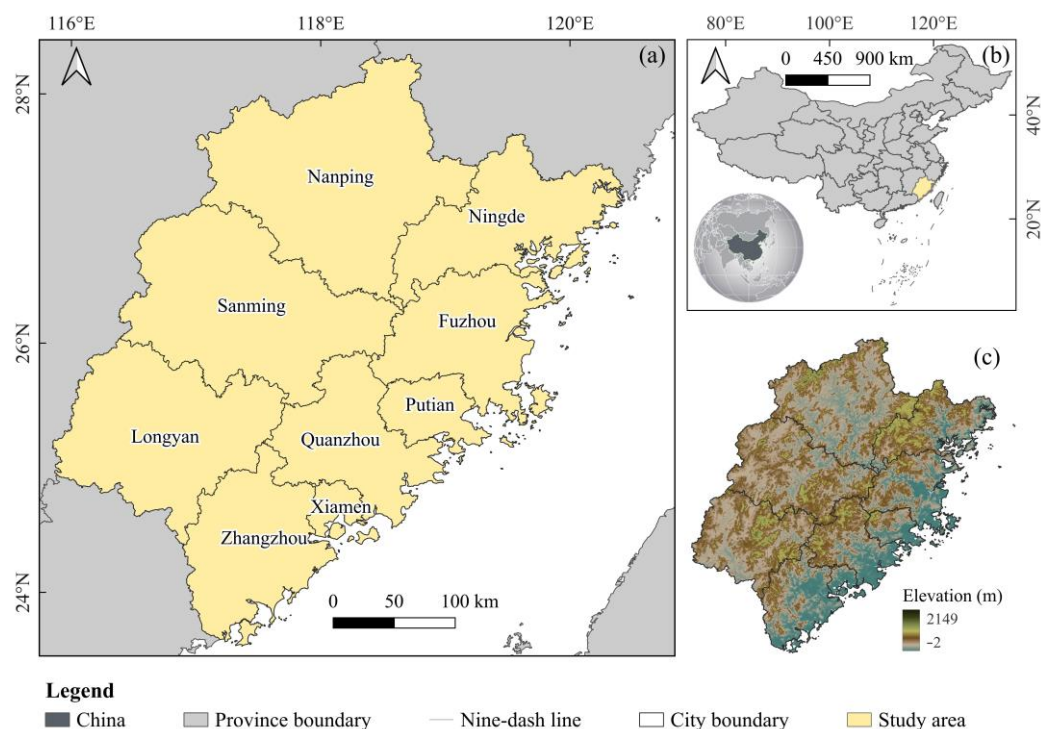


Figure 1. Geographical location of the study area (a) in China (b), and its elevation (c).

2.2. Materials

2.2.1. Sentinel-1 SAR Data

During and before the experiment, flood level -1 Ground Range Detected (GRD) image products in the Sentinel-1 IW mode were used to detect floods (Table 1). The Sentinel-1 images were freely downloaded from the European Space Agency (ESA) website (<https://scihub.copernicus.eu/dhus>, accessed on 23 January 2023) [34]. The GRD-mode SAR imagery includes two polarization modes, VH and VV, with a spatial resolution of 10 m. We used the Sentinel Application Platform (SNAP v 9.0) [35] software officially provided by the ESA for preprocessing to obtain the backscattering coefficient image covering the study area.

Table 1. Information of the dataset used in this study.

Data Source	Year (Month)	Spatial Resolution
Sentinel-1 GRD	2022 (3/5/6)	10 m
GPM V6	2022 (6)	0.1° × 0.1°
ESRI Land Cover (ESRI)	2022	10 m
ESA WorldCover (ESA)	2020	10 m
SRTM DEM	2017	30 m

2.2.2. Google Earth Images and Cropland Samples

The high spatial resolution remote sensing imagery used is the Google Earth 18th-level product with a spatial resolution of 0.6 m. Google satellite images were first downloaded via

Google Satellite service (<http://mt1.google.com>, accessed on 15 February 2022). The scale of the Google imagery downloaded is at the 18-level, which is approximately 0.6 m/pixel spatial resolution. The image data sources originated from multiple sensors, i.e., Worldview, GeoEye, and Aerial Photography. During cropland segmentation, the imagery is processed into WGS 1984 geographic coordinates. The geometric accuracy of Google imagery is approximately within 2 m [36]. The spatial resolution of Sentinel-1A data is 10 m. Therefore, the two datasets of Google imagery and Sentinel-1A were considered co-registered.

Randomly selected subregions of mountains and plains are based on Google Earth images. A total of 12,027 cropland plots were collected and distributed in both Fujian Province and the adjacent Guangdong Province. Samples were taken from the mountainous regions of Guangdong Province, where the cropland structure is similar to that of Fujian Province. All cropland plots were manually digitized; 70% of the cropland samples were used for training and 30% for validation. The locations of all samples and some details are shown in Figure 2.

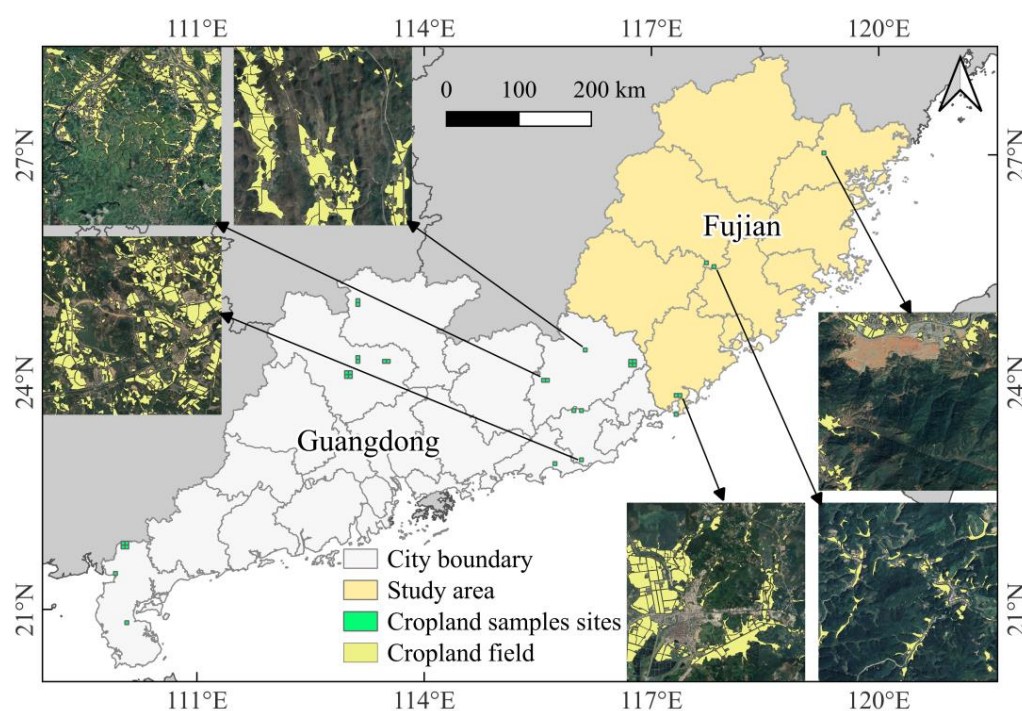


Figure 2. Distribution of cropland samples originating from both Fujian Province and Guangdong Province is presented in detail for a portion of it.

2.2.3. GPM Dataset

This study collected Global Precipitation Measurement (GPM) v6 data for Fujian Province in June 2022 and conducted summary statistics. The GPM is an international satellite mission with its core observing satellites jointly launched by NASA (the United States National Aeronautics and Space Administration) and JAXA (the Japan Aerospace Exploration Agency) on 27 February 2014 [37,38]. These data can be freely accessed on the NASA Data Center's official website (<https://urs.earthdata.nasa.gov/>, accessed on 10 July 2023). GPM provides global rainfall and snowfall observations every three hours [39]. The entire month of June's rainfall data were downloaded for flood analysis.

2.2.4. Land Cover Data

As a reference for cropland accuracy comparison, land cover information from the Environmental Systems Research Institute (ESRI) [40] and WorldCover from the European Space Agency (ESA) [41] were used. Both of these products are based on Sentinel data and have a spatial resolution of 10 m. ESRI land cover is a 2022 product, while the ESA World-

Cover is from 2020. Despite the two-year gap, only a small portion of cropland boundaries have changed [42], and the differences are not significant for the entire Fujian province.

2.2.5. DEM Data

DEM data were acquired from the Shuttle Radar Topography Mission (SRTM) with a spatial resolution of 30 m. In DEM analysis, areas with elevation variations under 30 m are classified as plains, while those with elevation variations over 30 m are classified as mountains. All the datasets we used are summarized in Table 1.

2.3. Methods

The technical route of this study is shown in Figure 3, consisting of three main components: (1) cropland extraction using PIDNet based on Google imagery; (2) flood extraction and cropland inundation mapping; and (3) accuracy evaluation.

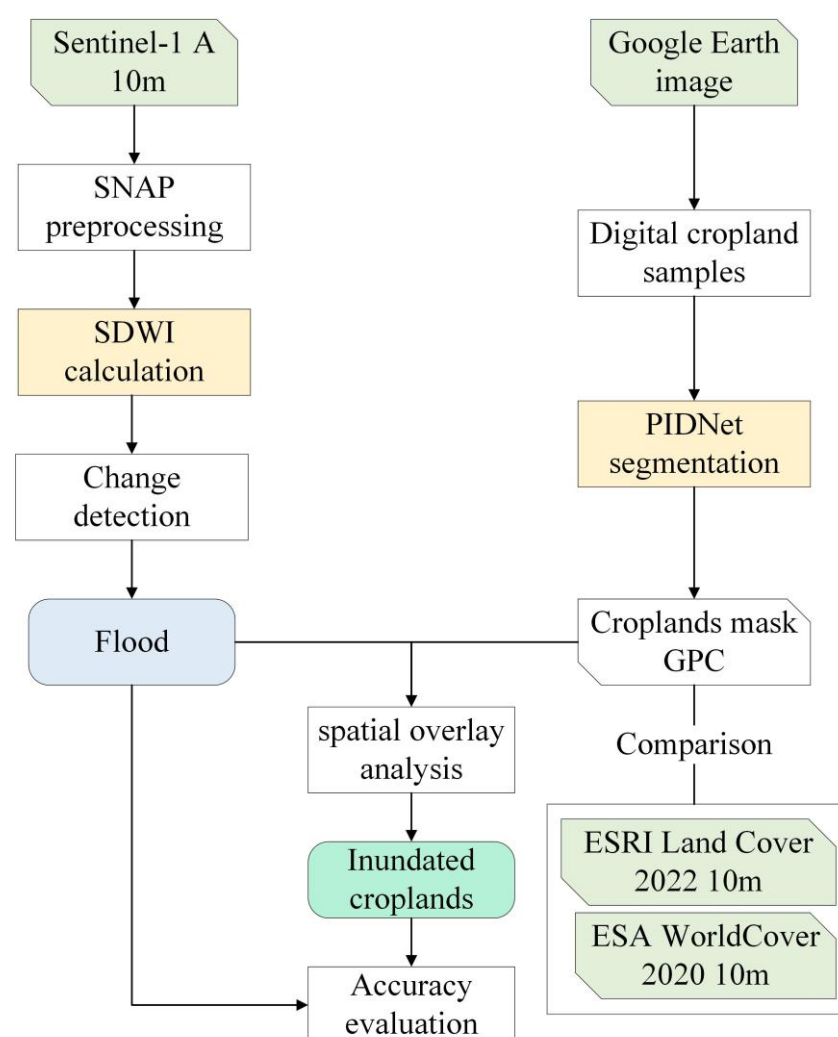


Figure 3. Flowchart of technical route.

2.3.1. Cropland Extraction Using PIDNet

The Proportional–Integral–Derivative Network (PIDNet) proposed by Jiacong Xu et al. in 2023 [43] is a real-time semantic segmentation network architecture based on attention guidance. It can fuse high-resolution spatial information and low-frequency context information while preserving image details. PIDNet uses pyramid dilated convolutions, which help capture multi-scale contextual information and improve segmentation accuracy. The PIDNet model architecture is shown in Figure 4. Unlike typical dual-branch network

architectures, it includes proportional (P) and integral (I) controller components and adds a derivative (D) controller component. The P controller focuses on the current signal, while the I controller accumulates all past signals. Due to the inertia effect of integration, simple PI controllers can exhibit overshooting when the signal changes in the opposite direction. As a result, a D controller is usually introduced to regulate this. When the signal decreases, the D component becomes negative, acting as a damper to prevent overshooting. In addition, S and B represent semantics and boundaries, Add and Up represent element summation and bilinear Upsampling operations, respectively. The pixel-attention-guided fusion module (Pag) parallelizes the new pyramid pooling module (PPM). The boundary-attention-guided fusion module (Bag) is used to smooth out detail and context. PID control usually shows better stability and robustness in the face of disturbances, which helps improve the stability of cropland extraction and reduce errors.

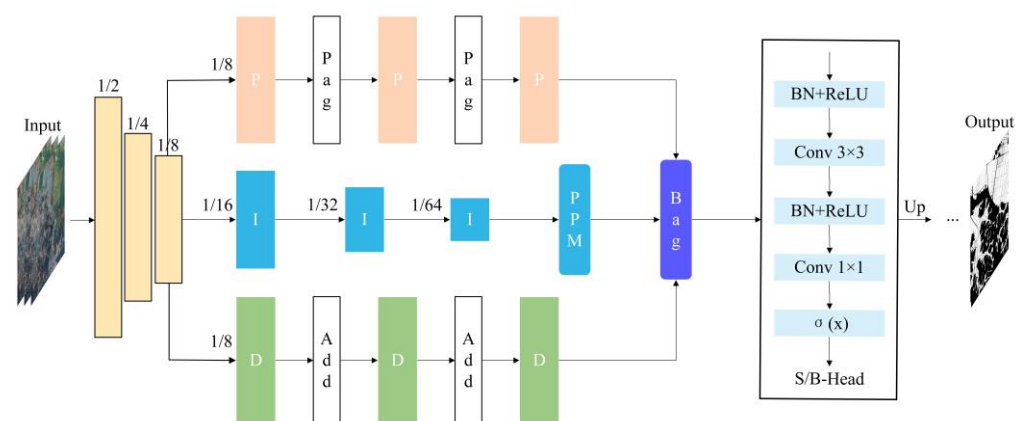


Figure 4. The overview of basic architecture of Proportional–Integral–Derivative Network (PIDNet). It includes proportional (P) and integral (I) controller components and adds a derivative (D) controller component. In addition, S and B represent semantics and boundaries, Add and Up represent element summation and bilinear Upsampling operations, respectively. The pixel-attention-guided fusion module (Pag) parallelizes the new pyramid pooling module (PPM).

The main idea of the PIDNet method in cropland extraction is to use a series of algorithms to classify each pixel to construct the boundaries of cropland. To test the semantic segmentation performance of the PIDNet model, the study first conducted pre-training on the ImageNet 11k dataset [44,45]. The ImageNet 11k dataset is a subset of the ImageNet project and includes 11,000 different image categories. For each trained model, the study used b2 training weights to shorten training time while maintaining accuracy. Then, the specific steps for cropland extraction based on Google Earth images are as follows: (1) digitization: using Google Earth images as the base map, organize manpower to manually mark and digitize cropland samples; (2) sample evaluation: according to each evaluation sample the number of type polygons and the proportion of their area in the total area of the study area facilitate the subsequent formulation of different training strategies; (3) sample pooling: use the above cropland samples as model input to perform global average pooling and pyramid pooling; (4) model training: use PIDNet deep learning model training to build a cropland plot prediction model and predict cropland boundary masks in Fujian Province. Finally, the cropland mask data GPC (Cropland extracted with Google imagery and PIDNet segmentation) was obtained.

2.3.2. Flood Extraction and Cropland Inundation Mapping

The study selected Sentinel-1 images from June and March 2022 to extract flood areas since there were no flood reports in March. The water bodies occurring in both June and March were considered non-flood, while water bodies in June that were not present in March were defined as floods. In order to represent the surface condition before and during

the disaster, images captured before and during the disaster were stitched together based on the maximum Sentinel-1 dual-polarized water index (SDWI). Computational Formula (1) of the SDWI is as follows:

$$\text{SDWI} = \ln(10 \times \text{VV} \times \text{VH}) - 8, \quad (1)$$

$$\text{DI} = \text{SDWI}_{\text{June}} - \text{SDWI}_{\text{March}}, \quad (2)$$

The flood disaster area was obtained by calculating the image difference of the before and during disaster SDWI results, as shown in Formula (2), where DI is the difference between them. Based on the different images, a threshold was applied to identify flood pixels. After adjusting multiple times, the best results were achieved when $\text{SDWI} > 0.7$ [30]. After flood mapping, the study focused on extracting inundated croplands based on the croplands mask.

2.3.3. Accuracy Assessment

The accuracy assessment of the results included two parts: (1) accuracy assessment and inter-comparison of cropland mask, and (2) accuracy assessment of flood.

In this study, Intersection over Union (IoU) was used to assess the accuracy of PIDNet's cropland mask extraction results based on the validation samples. In addition, in order to compare the performance of GPC with other cropland data, i.e., ESA and ESRI, we unified the resolution of each cropland layer to 10 m so that the GPC was upscaled from 0.6 m to 10 m resolution, and the accuracy of the cropland data was compared in two ways: (1) comparing the total area of cropland masks with official statistical data; (2) calculating the consistency of cropland mask data between plains and mountainous regions using IoU.

To obtain accurate flooding validation samples distributed in the study area, we collected the validation samples from RGB images synthesized by using multi-temporal SAR data. The RGB images were synthesized using RGB (red, green, and blue color model) based on the differences between images before and during the event, which has been proven to be effective in identifying floods in previous studies [13,46]. Validation samples were collected through systematic sampling using manual interpretation. In addition to the validation, we used Sentinel-2 imagery as auxiliary references to ensure the reliability of the validation samples. After several ground sampling distances (GSDs), we selected a distance of 0.1° to validate the flood maps because it provided a reasonable number of sample points. Then, we used Precision, Recall, and F1-score metrics to evaluate the accuracy of the results and the effectiveness of the cropland mask.

The calculation formulas for each indicator are as follows:

$$\text{IoU} = \text{TP} / (\text{TP} + \text{FP} + \text{FN}), \quad (3)$$

$$\text{Precision} = \text{TP} / (\text{TP} + \text{FP}), \quad (4)$$

$$\text{Recall} = \text{TP} / (\text{TP} + \text{FN}), \quad (5)$$

$$\text{F1-score} = 2 (\text{Precision} \cdot \text{Recall}) / (\text{Precision} + \text{Recall}), \quad (6)$$

Among these, TP represents true positives, and TN represents true negatives, both indicating correct cases. FP and FN are cases of misjudgment, with FP being a type II statistical error and FN being a type I statistical error. An algorithm's overall effectiveness can be evaluated by using the F1-score, which is the harmonic average of Precision and Recall. F-scores range from 0 to 1, with 1 indicating the best effect [47].

3. Results

3.1. Cropland Extraction Results

The results of cropland mapping were evaluated based on test sample sets, and the IoU was achieved to 89.38%, which indicated that the PIDNet model can accurately extract cropland. In addition, the extracted cropland mask of Fujian province was compared with

the two existing cropland data derived from ESA and ESRI land cover products, and the distribution of the three cropland results is shown in Figure 5.

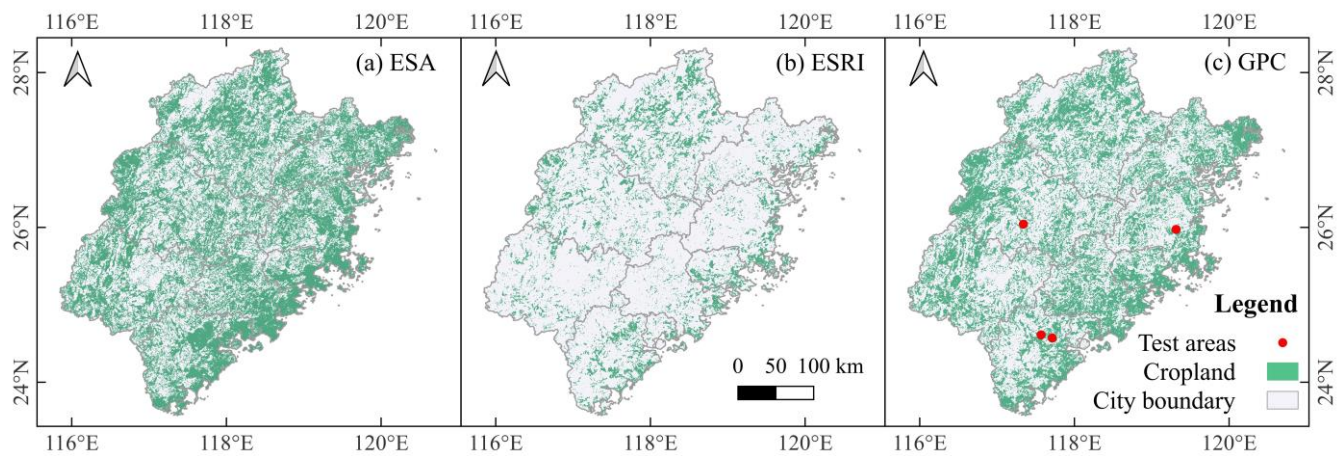


Figure 5. Distribution of the three cropland results, (a) the cropland from ESA, (b) the cropland from ESRI, and (c) our cropland product GPC (cropland extracted with Google imagery and PIDINet segmentation).

3.1.1. Cropland Spatial Distribution

The cropland mask extracted in this study can accurately extract cropland with spatial details, especially in areas of rugged terrain and fragmented crop parcels, while ESA and ESRI products have more misclassifications and omissions. Via visual interpretation, the study compared it with ESRI and ESA cropland classification data in terms of details. Figure 5 shows that the cropland results of ESRI had the smallest area, while the results of ESA and GPC were similar. Figure 6 shows the cropland details in four typical locations in the study area. It can be seen from Figure 6 that the ESA product offers more details (Figure 6e,g,h) and can correctly distinguish roads (Figure 6e,h) but includes more permanent water bodies than ESRI (Figure 6l). Mountainous areas and roads were misclassified as cropland by the ESRI product (Figure 6i,k), while GPC can better segment roads (Figure 6m), garden land (Figure 6o) and permanent water bodies (Figure 6m,p).

3.1.2. Statistics of Cropland Area

Table 2 shows three points of information. Firstly, the cropland areas in GPC, ESA, and ESRI are all lower than the statistical data. This is because orchards are also considered in official statistics but are not included in our definition of cropland. Secondly, among the three cropland classification results, GPC and ESA's area estimates are more reasonable. The GPC and ESA cropland areas account for 61.87% and 64.10% of the cropland area reported in Fujian Province's third national land survey in 2021 [48]. Cropland data from ESRI are severely underestimated, accounting for only 34.87% of the official statistics. Thirdly, in spite of the fact that ESA's results are higher than GPC, Figure 6f–h shows that some permanent water bodies and mountainous areas are included erroneously in ESA's results.

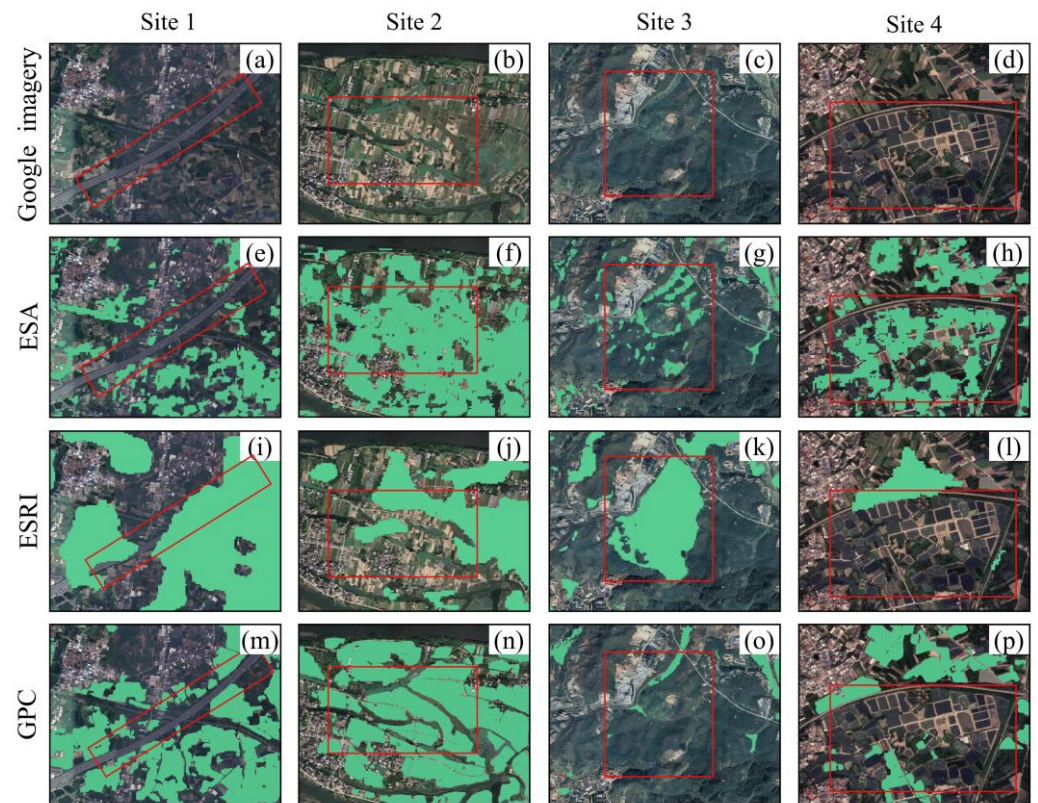


Figure 6. Visual comparison of cropland details for ESA (e–h), ESRI (i–l), and our cropland product GPC (m–p) with Google imagery (a–d) in four typical sites. The red boxes are the part with large differences in cropland results. i.e., roads, rivers, mountains and ponds.

Table 2. The area of 3 cropland data of Fujian compared with the official reported cropland area.

Statistics Data	Official Statistics	GPC	ESA	ESRI
Area (km ²)	9319.93	5766.30	5974.36	3249.49
Proportion (%)	100	61.87	64.10	34.87

3.1.3. Consistency Analysis

Based on terrain relief information, the consistency between the three cropland masks was analyzed (Table 3). The IoUs between the cropland classification results in plain areas are higher than in mountainous regions in rugged areas. In addition, the IoU between ESA and GPC is higher than that between ESRI and GPC.

Table 3. The IoU of the 3 croplands' data.

Terrain Relief	GPC-ESA	GPC-ESRI	ESA-ESRI
<30 m (plain)	54.49%	38.91%	36.17%
≥30 m (rugged)	43.20%	22.38%	23.25%

3.2. Flood Map and Accuracy Assessment

The results of the flood area (Figure 7a) and cropland inundation area (Figure 7b) extracted based on SDWI are shown in Figure 6, respectively. A considerable number of flood areas can be identified using SDWI, but they contain a large number of radar shadows (Figure 7c). After we superimposed the flood area with the GPC mask, the flooded cropland areas can be accurately extracted (Figure 7d). Additionally, due to the inconsistent acquisition times of the images, there were some jagged edges in the extraction

results (Figure 7a), which can be eliminated mostly using the cropland mask method proposed in this study.

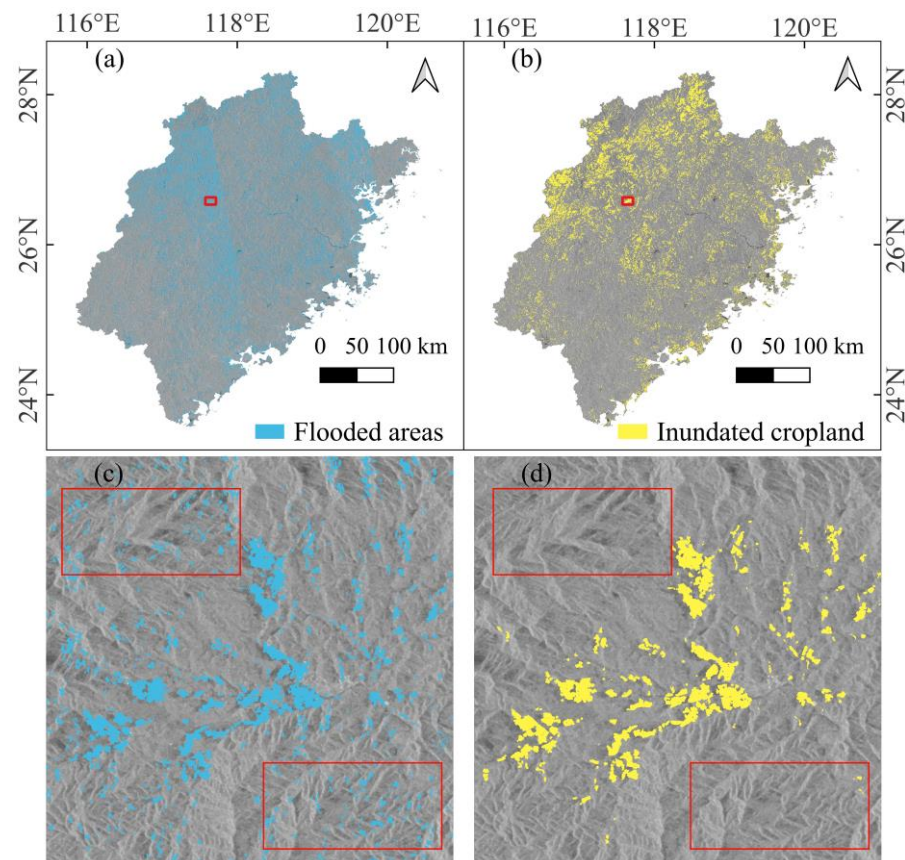


Figure 7. Flooded areas and inundated croplands distribution in June 2022. (a) Flood map; (b) cropland inundation map; (c) flooded areas without cropland mask filtering; (d) inundated croplands after filtering by using cropland mask. The red boxes shown that inundated croplands after filtering effectively filters the radar shadow.

We set the GSD to 0.1° and collected a total of 1105 sample points, which were divided into four categories: cropland non-flood area, inundated cropland area, non-cropland non-flood area, and non-cropland flood area (Figure 8). The F1-score of the flood extraction results before masking was 66.67%, while the F1-score for inundated croplands extraction after masking was 82.35% (Table 4). In the validation results, we found that the precision was higher than recall, which can be attributed to the conservative choice of the SDWI threshold. The low proportion of the flood area also influenced the results [49]. Overall, the research suggests that with a high-accuracy cropland mask product, filtered flood maps are reliable.

Table 4. Accuracy comparison of flood extraction results based on Sentinel-1 images and inundated cropland results after cropland masking.

Result	Precision	Recall	F1-Score
Flooded	81.95%	56.67%	66.67%
cropland Inundated	100%	70%	82.35%

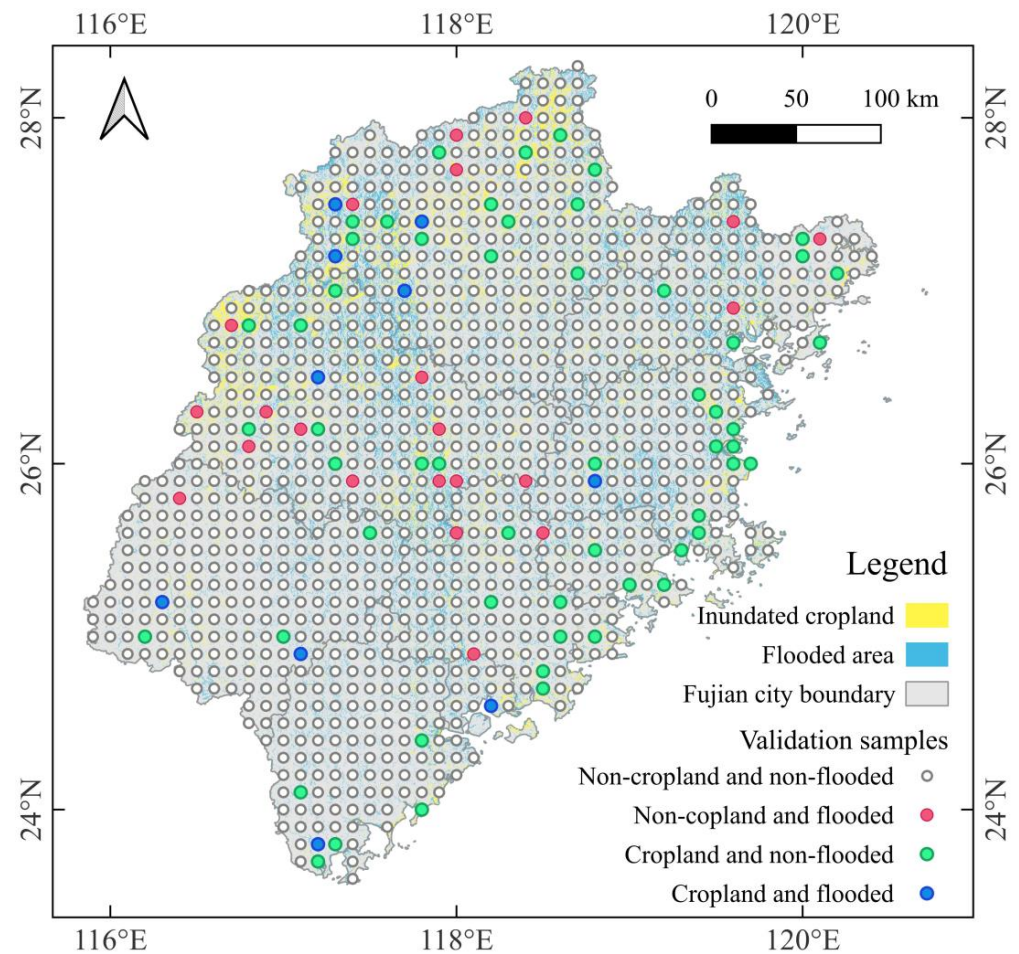


Figure 8. Flood validation sample distribution. The result of flooded areas and inundated croplands overlaying with the collected sample locations.

3.3. Flood Event Analysis

We performed summary statistics and visualized the daily GPM rainfall data in June 2022 (Figure 9). Overlaying these extracted inundated croplands results, it can be seen that they match quite well. It was found from the rainfall data that in Fujian Province in June, rainfall was mainly concentrated in the northwest region, with the highest rainfall observed in Sanming and Nanping. In the southern part, rainfall was lower, which is consistent with our research results. Additionally, there was evidence of rainfall in the central part of Fuzhou, but our results did not detect it. Due to the limited revisit period of 6–12 days, Sentinel-1 data returns may not be available during heavy rainstorms [50].

To better understand how the recent rainfall has affected cropland in different cities of Fujian Province, the study overlaid the inundated cropland extent with administrative boundaries and conducted spatial analysis and geo-statistics by city (Figure 10). Summary statistics of the affected cropland area and monthly rainfall of each city are provided. According to the study's findings, regions in northern Fujian, such as Nanping and Sanming cities, were severely affected, which aligns with the rainfall data. Although there may be some discrepancies in the order of cities based on total monthly rainfall as compared to cropland damage, the overall trends remain the same. The study determined that a total of 254.88 km² of cropland was affected. Among the affected areas, Nanping, Sanming, and Fuzhou had the largest areas of cropland damage, accounting for 82.21% of the total cropland damage in the province.

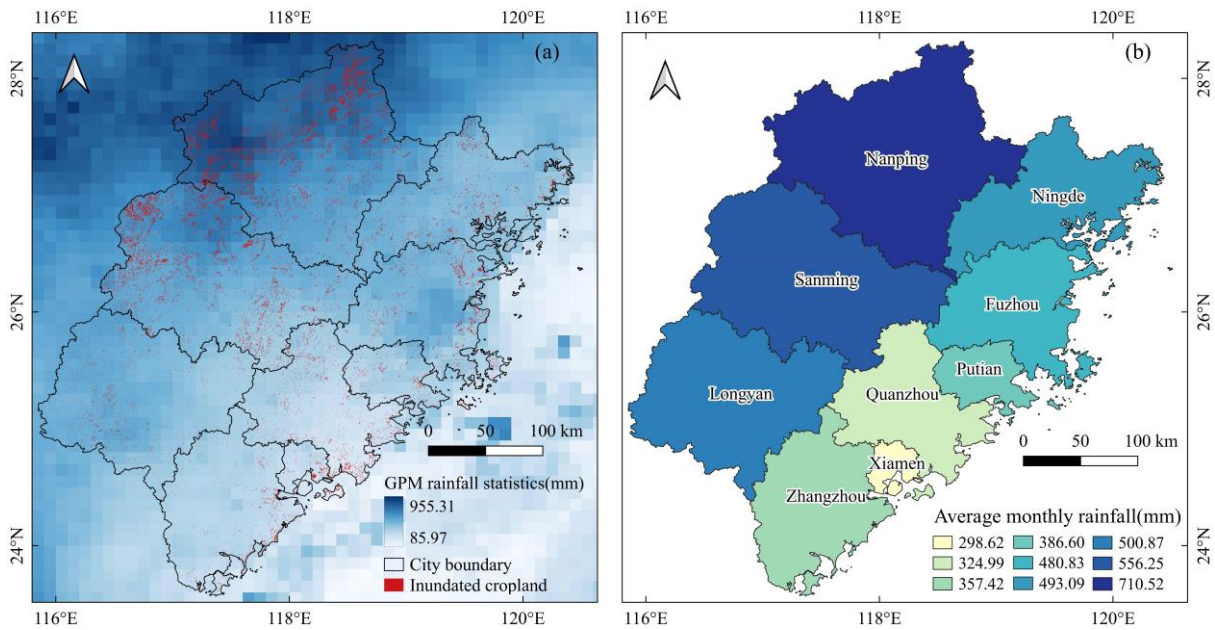


Figure 9. (a) June statistical results of Global Precipitation Measurement V6 data, superimposed with the results of studying inundated cropland, the shade of blue represents the total monthly rainfall of each pixel block; (b) the city’s monthly average rainfall, the shade of red represents the total monthly rainfall for the region.

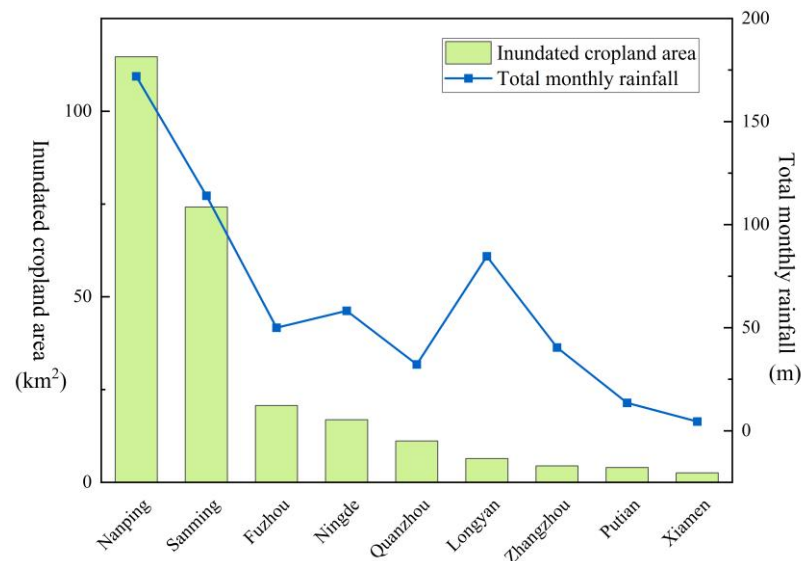


Figure 10. The area of inundated cropland (km²) and total monthly rainfall (m) statistics according to GPM in each city of Fujian Province.

4. Discussion

4.1. Croplands Extraction Based on Deep Learning

Based on Google Earth imagery, this study employed PIDNet to extract cropland masks in Fujian Province and developed a comprehensive methodology for identifying inundated cropland events in mountainous areas. The rugged terrain and complex cropland patterns pose challenges for traditional 10–30 m spatial resolution products, which may fail to capture many crop parcels [47,51]. In contrast, the sub-meter-level extraction helps capture these fine-grained cropland units while eliminating noise interference from radar shadows and permanent water bodies. The cropland identification results were upscaled to fit the flood map at 10 m resolution. Several typical locations were selected to compare the

performance of cropland results (Figure 11). In Fujian Province, cropland plots are relatively fragmented, and plain areas are relatively concentrated. It can be seen that the extraction effect of flat cropland plots (Figure 11a,c) is better than terraced fields (Figure 11b,d). For the bare land (Figure 11e) and garden land (Figure 11f), the three cropland products can be well identified as non-cropland. ESRI has omissions (Figure 11d,f); the cropland extraction results of GPC and ESA have obvious advantages in detail.

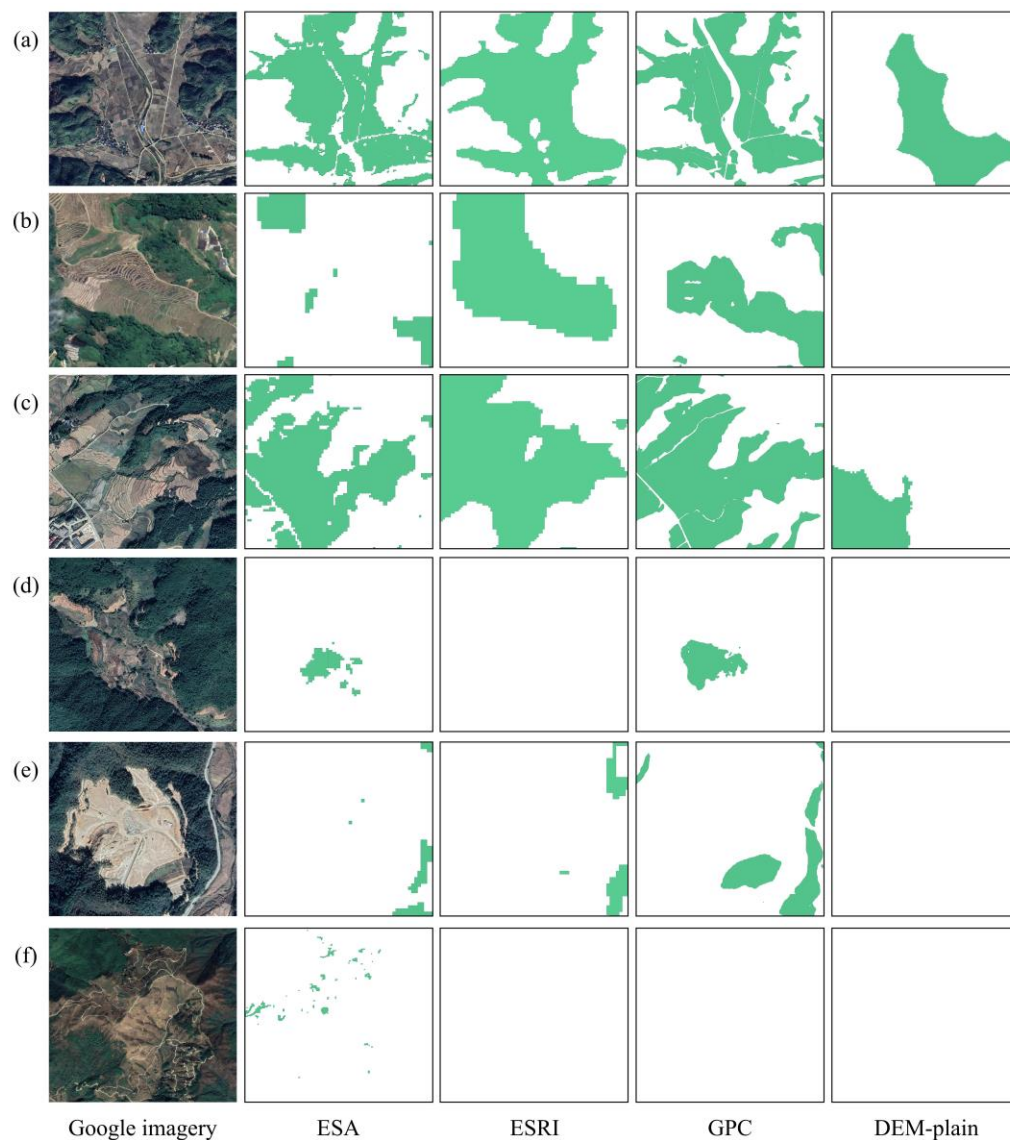


Figure 11. Zoom-in illustration of the extraction effects of different cropland products in mountainous and plain areas. DEM-plain is an area with terrain relief less than 30 m. (a–c) are plain areas, (d) is cropland in areas with high terrain, (e) is bare land, and (f) is garden land.

Deep learning models rely heavily on labeled samples [6,52,53]. To ensure consistency between the samples and labels, this study used a manual digital approach to acquire cropland plots and eliminate the misguidance of non-cropland samples. However, due to the diversity of crop types and variations in their appearance in imagery, it is necessary to include diverse examples in the training dataset to ensure that the model generalizes well. This entails covering various regions, crop types, phenological stages, post-harvest scenarios, and more. A shortage of training samples may impact the accuracy of the study [54,55]. Therefore, efforts will be made to increase the sample data to provide a more

accurate mapping of mountainous croplands, which is essential for disaster assessment, flood monitoring, and mountain cropland management.

4.2. Uncertainty in Flood Extraction

Remote sensing data are widely used in large-scale water extraction. In contrast to optical images, SAR data are not affected by clouds and are a very effective data source in cloudy mountainous areas [30]. SDWI combines different polarization data and is an effective technical means to extract large areas of water.

This study used SDWI combined with CD to extract floods. After applying the cropland mask, the F1 score accuracy reached 82.35%. The recall was 70%, indicating a certain degree of underestimation during water body extraction. It might be associated with the diverse topography in Fujian, primarily characterized by mountains and hills [42]. The province has relatively narrow rivers and water levels are low, failing to accurately detect some water bodies. Furthermore, floods recede rapidly, and the SAR data revisit time of 6–12 days may result in flood events being missed [45]. To address these issues, future improvements will focus on utilizing other radar data sources, such as GF-3 data, to generate time series observations for enhanced disaster monitoring capabilities. At last, there was a lack of measured data in the study. In the future study of flood events, we will consider using the unoccupied airborne system (UAS) to take useful measured data as far as possible during or after the flood to verify the results [56], which will also make the results more reliable.

4.3. Impact of Flood Events on Crops

Flood disasters, especially flash floods, are a common phenomenon in Fujian Province; approximately 95% of the land area and 84% of the population are threatened by flash floods [57]. The occurrence of floods has hindered crop production and caused considerable damage [58,59]. Crop damage or destruction due to flooding is estimated to account for 57% of all natural disaster crop losses [59]. Using remote sensing and artificial intelligence technology to quickly and automatically extract the extent of cropland inundation is an important technical means for emergency response to cropland disasters.

The study's findings reveal that the 2022 precipitation in Fujian Province led to approximately 254.88 km² of cropland being inundated. The most severely affected areas were in the northwestern regions, particularly in Nanping and Sanming cities. Rice is the primary crop cultivated in these two cities, and June is a critical period for rice cultivation [60]. Therefore, it is crucial to implement effective flood defense measures and focus on post-disaster cropland drainage and recovery to mitigate the impact of flooding on agricultural production. The phenological stages of different crops are different, causing them to be affected by floods to varying degrees. Our follow-up study will consider further refined classification of crops in Fujian province to evaluate the sensitivity of different crops to flooding in depth.

5. Conclusions

This study proposed a method for inundated cropland mapping using high-precision cropland masks and SAR imagery, addressing the challenges of SAR-based cropland inundation monitoring in rugged terrain. The results showed that the proposed cropland mask outperformed the existing products in terms of accuracy and spatial details, especially in mountainous areas. The flood event we studied was in June 2022 in Fujian Province, China. This article reveals that Sentinel-1 SAR data combined with high-precision cropland mask data can be used to map cropland inundation ranges with an F-score of 82.35%, which provides reliable information for inundated cropland mapping. Furthermore, this flood was mainly concentrated in the northwest of Fujian Province, causing a great impact on local cropland. These results demonstrated that this approach provides a practical and accurate solution for inundated cropland mapping. The generated inundated cropland

map can serve as crucial data support for emergency response agencies and agricultural insurance loss assessment work.

Author Contributions: Conceptualization, M.K.; Methodology, K.J.; Software, H.J.; Validation, X.D. and J.X.; Formal analysis, D.L.; Investigation, C.W.; Data curation, X.D. and B.Q.; Writing—original draft preparation, M.K.; Writing—review and editing, H.J. and D.L.; Visualization, M.K.; Supervision, H.J.; Funding acquisition, H.J. All authors have read and agreed to the published version of the manuscript.

Funding: This research was funded by GDAS' Project of Science and Technology Development (No. 2022GDASZH-2022010102; 2021GDASYL-20210103003), National Natural Science Foundation of China (No. 42071417), Guangdong Province Agricultural Science and Technology Innovation and Promotion Project (No. 2023KJ102), the Open Research Fund of Beijing Key Laboratory of Big Data Technology for Food Safety (No. BTBD-2021KF07), and Beijing Technology and Business University.

Data Availability Statement: The data used to support the findings of this study are included in this article.

Conflicts of Interest: The authors declare no conflicts of interest.

References

- Uddin, M.J.; Hooda, P.S.; Mohiuddin, A.S.M.; Smith, M.; Waller, M. Land inundation and cropping intensity influences on organic carbon in the agricultural soils of Bangladesh. *CATENA* **2019**, *178*, 11–19. [\[CrossRef\]](#)
- Richter, B.D.; Ao, Y.; Lamsal, G.; Wei, D.; Amaya, M.; Marston, L.; Davis, K.F. Alleviating water scarcity by optimizing crop mixes. *Nat. Water* **2023**, *1*, 1035–1047. [\[CrossRef\]](#)
- Baas, S.; Trujillo, M.; Lombardi, N. *Impact of Disasters on Agriculture and Food Security*; FAO: Rome, Italy, 2015.
- Singha, M.; Dong, J.; Sarmah, S.; You, N.; Zhou, Y.; Zhang, G.; Doughty, R.; Xiao, X. Identifying floods and flood-affected paddy rice fields in Bangladesh based on Sentinel-1 imagery and Google Earth Engine. *ISPRS J. Photogramm. Remote Sens.* **2020**, *166*, 278–293. [\[CrossRef\]](#)
- Zhao, G.; Pang, B.; Xu, Z.; Yue, J.; Tu, T. Mapping flood susceptibility in mountainous areas on a national scale in China. *Sci. Total Environ.* **2018**, *615*, 1133–1142. [\[CrossRef\]](#)
- Mayer, T.; Poortinga, A.; Bhandari, B.; Nicolau, A.P.; Markert, K.; Thwal, N.S.; Markert, A.; Haag, A.; Kilbride, J.; Chishtie, F.; et al. Deep learning approach for Sentinel-1 surface water mapping leveraging Google Earth Engine. *ISPRS Open J. Photogramm. Remote Sens.* **2021**, *2*, 100005. [\[CrossRef\]](#)
- Tong, X.; Luo, X.; Liu, S.; Xie, H.; Chao, W.; Liu, S.; Liu, S.; Makhinov, A.N.; Makhinova, A.F.; Jiang, Y. An approach for flood monitoring by the combined use of Landsat 8 optical imagery and COSMO-SkyMed radar imagery. *ISPRS J. Photogramm. Remote Sens.* **2018**, *136*, 144–153. [\[CrossRef\]](#)
- Feyisa, G.L.; Meilby, H.; Fensholt, R.; Proud, S.R. Automated Water Extraction Index: A new technique for surface water mapping using Landsat imagery. *Remote Sens. Environ.* **2014**, *140*, 23–35. [\[CrossRef\]](#)
- Martinis, S.; Plank, S.; Ćwik, K. The Use of Sentinel-1 Time-Series Data to Improve Flood Monitoring in Arid Areas. *Remote Sens.* **2018**, *10*, 583. [\[CrossRef\]](#)
- Uddin, K.; Matin, M.A.; Meyer, F.J. Operational Flood Mapping Using Multi-Temporal Sentinel-1 SAR Images: A Case Study from Bangladesh. *Remote Sens.* **2019**, *11*, 1581. [\[CrossRef\]](#)
- Klemas, V. Remote Sensing of Floods and Flood-Prone Areas: An Overview. *J. Coast. Res.* **2015**, *314*, 1005–1013. [\[CrossRef\]](#)
- Dasgupta, A.; Grimaldi, S.; Ramsankaran, R.; Pauwels, V.R.; Walker, J.P. Towards operational SAR-based flood mapping using neuro-fuzzy texture-based approaches. *Remote Sens. Environ.* **2018**, *215*, 313–329. [\[CrossRef\]](#)
- Carreño Conde, F.; De Mata Muñoz, M. Flood Monitoring Based on the Study of Sentinel-1 SAR Images: The Ebro River Case Study. *Water* **2019**, *11*, 2454. [\[CrossRef\]](#)
- McCormack, T.; Companyà, J.; Naughton, O. A methodology for mapping annual flood extent using multi-temporal Sentinel-1 imagery. *Remote Sens. Environ.* **2022**, *282*, 113273. [\[CrossRef\]](#)
- Dasgupta, A.; Grimaldi, S.; Ramsankaran, R.; Pauwels, V.R.; Walker, J.P.; Chini, M.; Hostache, R.; Matgen, P. Flood mapping using synthetic aperture radar sensors from local to global scales. In *Global Flood Hazard: Applications in Modeling, Mapping, and Forecasting*; John Wiley & Sons, Inc.: Hoboken, NJ, USA, 2018; pp. 55–77.
- Schlaffer, S.; Chini, M.; Giustarini, L.; Matgen, P. Probabilistic mapping of flood-induced backscatter changes in SAR time series. *Int. J. Appl. Earth Obs. Geoinf.* **2017**, *56*, 77–87. [\[CrossRef\]](#)
- Tavus, B.; Kocaman, S.; Gokceoglu, C.; Nefeslioglu, H.A. Considerations on the use of Sentinel-1 data in flood mapping in urban areas: Ankara (Turkey) 2018 floods. *Int. Arch. Photogramm. Remote Sens. Spat. Inf. Sci.* **2018**, *42*, 575–581. [\[CrossRef\]](#)
- Shrestha, R.; Di, L.; Yu, E.G.; Kang, L.; Shao, Y.-z.; Bai, Y.-q. Regression model to estimate flood impact on corn yield using MODIS NDVI and USDA cropland data layer. *J. Integr. Agric.* **2017**, *16*, 398–407. [\[CrossRef\]](#)

19. Zhang, M.; Liu, D.; Wang, S.; Xiang, H.; Zhang, W. Multisource Remote Sensing Data-Based Flood Monitoring and Crop Damage Assessment: A Case Study on the 20 July 2021 Extraordinary Rainfall Event in Henan, China. *Remote Sens.* **2022**, *14*, 5771. [CrossRef]
20. Soliman, M.; Morsy, M.M.; Radwan, H.G. Assessment of Implementing Land Use/Land Cover LULC 2020-ESRI Global Maps in 2D Flood Modeling Application. *Water* **2022**, *14*, 3963. [CrossRef]
21. Qin, X.; Shi, Q.; Wang, D.; Su, X. Inundation Impact on Croplands of 2020 Flood Event in Three Provinces of China. *IEEE J. Sel. Top. Appl. Earth Obs. Remote Sens.* **2022**, *15*, 3179–3189. [CrossRef]
22. Zhang, C.; Dong, J.; Ge, Q. Quantifying the accuracies of six 30-m cropland datasets over China: A comparison and evaluation analysis. *Comput. Electron. Agric.* **2022**, *197*, 106946. [CrossRef]
23. TD/T 1033-2012; Chinese Standard for Construction of High Standard Basic Farmland. Ministry of Land and Resources: Beijing, China, 2012.
24. Pulvirenti, L.; Chini, M.; Pierdicca, N.; Boni, G. Use of SAR data for detecting floodwater in urban and agricultural areas: The role of the interferometric coherence. *IEEE Trans. Geosci. Remote Sens.* **2015**, *54*, 1532–1544. [CrossRef]
25. Amitrano, D.; Di Martino, G.; Iodice, A.; Riccio, D.; Ruello, G. Unsupervised Rapid Flood Mapping Using Sentinel-1 GRD SAR Images. *IEEE Trans. Geosci. Remote Sens.* **2018**, *56*, 3290–3299. [CrossRef]
26. Tanguy, M.; Chokmani, K.; Bernier, M.; Poulin, J.; Raymond, S. River flood mapping in urban areas combining Radarsat-2 data and flood return period data. *Remote Sens. Environ.* **2017**, *198*, 442–459. [CrossRef]
27. Cian, F.; Marconcini, M.; Ceccato, P. Normalized Difference Flood Index for rapid flood mapping: Taking advantage of EO big data. *Remote Sens. Environ.* **2018**, *209*, 712–730. [CrossRef]
28. Samat, A.; Gamba, P.; Du, P.; Luo, J. Active extreme learning machines for quad-polarimetric SAR imagery classification. *Int. J. Appl. Earth Obs. Geoinf.* **2015**, *35*, 305–319. [CrossRef]
29. Jia, S.; Xue, D.; Li, C.; Zheng, J.; Li, W. Study on new method for water area information extraction based on Sentinel-1 data. *Yangtze River* **2019**, *50*, 213–217.
30. Du, Q.; Li, G.; Chen, D.; Qi, S.; Zhou, Y.; Wang, F.; Cao, Y. Extracting water body data based on SDWI and threshold segmentation: A case study in permafrost area surrounding Salt Lake in Hoh Xil, Qinghai-Tibet Plateau, China. *Res. Cold Arid Reg.* **2023**, *15*, 202–209. [CrossRef]
31. Li, L.; Su, H.; Du, Q.; Wu, T. A novel surface water index using local background information for long term and large-scale Landsat images. *ISPRS J. Photogramm. Remote Sens.* **2021**, *172*, 59–78. [CrossRef]
32. Shen, X.; Wang, D.; Mao, K.; Anagnostou, E.; Hong, Y. Inundation Extent Mapping by Synthetic Aperture Radar: A Review. *Remote Sens.* **2019**, *11*, 879. [CrossRef]
33. Continuous Heavy Rainfall Caused Agricultural Losses Exceeding 1.6 Billion Yuan, Fujian Province accelerated Post-Disaster Production Recovery. Available online: <https://m.gmw.cn> (accessed on 3 October 2023).
34. Torres, R.; Snoeij, P.; Geudtner, D.; Bibby, D.; Davidson, M.; Attema, E.; Potin, P.; Rommen, B.; Floury, N.; Brown, M. GMES Sentinel-1 mission. *Remote Sens. Environ.* **2012**, *120*, 9–24. [CrossRef]
35. Zuhlke, M.; Fomferra, N.; Brockmann, C.; Peters, M.; Veci, L.; Malik, J.; Regner, P. SNAP (Sentinel Application Platform) and the ESA Sentinel 3 Toolbox. *Sentin.-3 Sci. Workshop* **2015**, *734*, 21.
36. Cheng, P.; Chaapel, C. Pan-sharpening and geometric correction: Worldview-2 satellite. *GeoInformatics* **2010**, *13*, 30.
37. Hou, A.Y.; Kakar, R.K.; Neeck, S.; Azarbarzin, A.A.; Kummerow, C.D.; Kojima, M.; Oki, R.; Nakamura, K.; Iguchi, T. The global precipitation measurement mission. *Bull. Am. Meteorol. Soc.* **2014**, *95*, 701–722. [CrossRef]
38. Liu, Z. Comparison of integrated multisatellite retrievals for GPM (IMERG) and TRMM multisatellite precipitation analysis (TMPA) monthly precipitation products: Initial results. *J. Hydrometeorol.* **2016**, *17*, 777–790. [CrossRef]
39. Pradhan, R.K.; Markonis, Y.; Godoy, M.R.V.; Villalba-Pradas, A.; Andreadis, K.M.; Nikolopoulos, E.I.; Papalexiou, S.M.; Rahim, A.; Tapiador, F.J.; Hanel, M. Review of GPM IMERG performance: A global perspective. *Remote Sens. Environ.* **2022**, *268*, 112754. [CrossRef]
40. Karra, K.; Kontgis, C.; Statman-Weil, Z.; Mazzariello, J.C.; Mathis, M.; Brumby, S.P. Global Land Use/Land Cover with Sentinel 2 and Deep Learning. In Proceedings of the 2021 IEEE International Geoscience and Remote Sensing Symposium IGARSS, Brussels, Belgium, 11–16 July 2021; pp. 4704–4707.
41. Zanaga, D.; Van De Kerchove, R.; De Keersmaecker, W.; Souverijns, N.; Brockmann, C.; Quast, R.; Wevers, J.; Grosu, A.; Paccini, A.; Vergnaud, S. ESA WorldCover 10 m 2020 v100. Available online: <https://viewer.esa-worldcover.org/worldcover> (accessed on 15 June 2023).
42. Chen, J. Agriculture. In *Fujian Statistical Yearbook—2022*; China Statistics Press: Beijing, China, 2022.
43. Xu, J.; Xiong, Z.; Bhattacharyya, S.P. PIDNet: A Real-Time Semantic Segmentation Network Inspired by PID Controllers. In Proceedings of the IEEE/CVF Conference on Computer Vision and Pattern Recognition, Vancouver, BC, Canada, 18–22 June 2023; pp. 19529–19539.
44. Pournaras, A.; Gkalelis, N.; Galanopoulos, D.; Mezaris, V. Exploiting Out-of-Domain Datasets and Visual Representations for Image Sentiment Classification. In Proceedings of the 2021 16th International Workshop on Semantic and Social Media Adaptation & Personalization (SMAP), Washington, DC, USA, 4–5 November 2021; pp. 1–6.
45. Wu, B.; Chen, W.; Fan, Y.; Zhang, Y.; Hou, J.; Liu, J.; Zhang, T. Tencent ml-images: A large-scale multi-label image database for visual representation learning. *IEEE Access* **2019**, *7*, 172683–172693. [CrossRef]

46. Refice, A.; Capolongo, D.; Pasquariello, G.; D’Addabbo, A.; Bovenga, F.; Nutricato, R.; Lovergine, F.P.; Pietranera, L. SAR and InSAR for Flood Monitoring: Examples With COSMO-SkyMed Data. *IEEE J. Sel. Top. Appl. Earth Obs. Remote Sens.* **2014**, *7*, 2711–2722. [[CrossRef](#)]
47. Masoud, K.M.; Persello, C.; Tolpekin, V.A. Delineation of agricultural field boundaries from Sentinel-2 images using a novel super-resolution contour detector based on fully convolutional networks. *Remote Sens.* **2019**, *12*, 59. [[CrossRef](#)]
48. Main Data Bulletin of the Third Land Survey of Fujian Province. Available online: <http://zrzyt.fujian.gov.cn> (accessed on 11 October 2023).
49. Liang, J.; Liu, D. A local thresholding approach to flood water delineation using Sentinel-1 SAR imagery. *ISPRS J. Photogramm. Remote Sens.* **2020**, *159*, 53–62. [[CrossRef](#)]
50. Guan, H.; Huang, J.; Li, L.; Li, X.; Miao, S.; Su, W.; Ma, Y.; Niu, Q.; Huang, H. Improved Gaussian mixture model to map the flooded crops of VV and VH polarization data. *Remote Sens. Environ.* **2023**, *295*, 113714. [[CrossRef](#)]
51. Li, Z.; Chen, S.; Meng, X.; Zhu, R.; Lu, J.; Cao, L.; Lu, P. Full Convolution Neural Network Combined with Contextual Feature Representation for Cropland Extraction from High-Resolution Remote Sensing Images. *Remote Sens.* **2022**, *14*, 2157. [[CrossRef](#)]
52. Mikołajczyk, A.; Grochowski, M. *Data Augmentation for Improving Deep Learning in Image Classification Problem*; IEEE: Washington, DC, USA, 2018; pp. 117–122.
53. Kaushal, V.; Iyer, R.; Kothawade, S.; Mahadev, R.; Doctor, K.; Ramakrishnan, G. *Learning from Less Data: A Unified Data Subset Selection and Active Learning Framework for Computer Vision*; IEEE: Washington, DC, USA, 2019; pp. 1289–1299.
54. Wang, H.; Zhang, X.; Hu, Y.; Yang, Y.; Cao, X.; Zhen, X. *Few-Shot Semantic Segmentation with Democratic Attention Networks*; Springer: Berlin/Heidelberg, Germany, 2020; pp. 730–746.
55. Olofsson, P.; Foody, G.M.; Herold, M.; Stehman, S.V.; Woodcock, C.E.; Wulder, M.A. Good practices for estimating area and assessing accuracy of land change. *Remote Sens. Environ.* **2014**, *148*, 42–57. [[CrossRef](#)]
56. Lippitt, C.D.; Zhang, S. The impact of small unmanned airborne platforms on passive optical remote sensing: A conceptual perspective. *Int. J. Remote Sens.* **2018**, *39*, 4852–4868. [[CrossRef](#)]
57. Xiong, J.; Pang, Q.; Fan, C.; Cheng, W.; Ye, C.; Zhao, Y.; He, Y.; Cao, Y. Spatiotemporal Characteristics and Driving Force Analysis of Flash Floods in Fujian Province. *ISPRS Int. J. Geo-Inf.* **2020**, *9*, 133. [[CrossRef](#)]
58. Chen, H.; Liang, Q.; Liang, Z.; Liu, Y.; Xie, S. Remote-sensing disturbance detection index to identify spatio-temporal varying flood impact on crop production. *Agric. For. Meteorol.* **2019**, *269*, 180–191. [[CrossRef](#)]
59. Fao, F. *The Impact of Disasters and Crises on Agriculture and Food Security*; FAO: Rome, Italy, 2018.
60. He, Y.; Dong, J.; Liao, X.; Sun, L.; Wang, Z.; You, N.; Li, Z.; Fu, P. Examining rice distribution and cropping intensity in a mixed single-and double-cropping region in South China using all available Sentinel 1/2 images. *Int. J. Appl. Earth Obs. Geoinf.* **2021**, *101*, 102351. [[CrossRef](#)]

Disclaimer/Publisher’s Note: The statements, opinions and data contained in all publications are solely those of the individual author(s) and contributor(s) and not of MDPI and/or the editor(s). MDPI and/or the editor(s) disclaim responsibility for any injury to people or property resulting from any ideas, methods, instructions or products referred to in the content.